The Optimized Small Incidence Angle Setting of a Composite Bragg Scattering Model and its Application to Sea Surface Wind Speed Retrieval

Xiaomin Ye, Mingsen Lin, *Member, IEEE*, Qingtao Song, and Qimao Wang

***Abstract*—The normalized radar cross section (NRCS) of microwave backscattering from a rough sea surface can be described by a composite Bragg scattering (CBS) model, which is a combination of a two-scale backscatter model and a geometric optics model. For small local radar incidence angles that are smaller than a given angle setting, the two-scale backscattering mechanism of the sea surface is replaced by a geometric optics solution for specular reflection. In this study, an optimized setting of 18 degrees for the small incidence angle is determined by comparing the NRCSs between 52 RADARSAT-2 (R2) synthetic aperture radar (SAR) images and the CBS model with simultaneous sea surface wind derived by meteorological mooring buoys located in the northern South China Sea. By using the CBS model with the optimized incidence angle setting of 18° and the nearly simultaneous wind directions of the Advanced Scatterometer (ASCAT) as the input, sea surface wind speeds are retrieved from 46 R2 SAR images at C-band and from 2 COSMO-SkyMed (CSK) SAR images at X-band for the application study. The average root mean square error of the C-band R2 SAR retrieval results validated against nearly simultaneous measurements of ASCAT is 1.5 m/s, while the same value is 1.6 m/s for the X-band CSK SAR image. The results also indicate that the optimized small incidence angle setting of the CBS model found in this study is relatively reliable under sea surface wind speed conditions less than 14.0 m/s.**

***Index Terms*—Composite Bragg scattering (CBS) model, small incidence angle, sea surface wind retrieval, synthetic aperture radar (SAR).**

I. Introduction

SEA surface wind speeds can be retrieved from the normalized radar cross sections (NRCSs) of synthetic aperture radar (SAR) images by using a geophysical model function (GMF) and atmospheric wind directions. In the microwave frequency of C-band, the GMFs of CMOD4 [1], CMOD-IFR2 [2], CMOD5 [3], CMOD5.N [4], and CMOD7 [5] for microwave scatterometers are widely used in the retrieval of coastal winds and sea winds from hurricanes/typhoons in SAR images with a high spatial resolution (e.g., [6]–[10]). At other microwave frequencies, some GMFs are also developed for sea wind retrieval from SARs. XMOD, a GMF for X-band, is used for sea wind retrieval from TerraSAR-X, TanDEM-X, SIR-C/X-SAR, and COSMO-SkyMed (CSK) SAR data [11]–[14]. GMFs for L-band named LMOD was also developed using Japanese Earth Resources Satellite-1 and soil moisture active passive L-band SAR images [15], [16]. The GMF relates the NRCS to sea surface winds with the parameters of frequency, polarization, and sensor/sea surface geometry (i.e., the azimuth, wind direction, and incident angle of the radar wave). For wind retrieval, we must choose a suitable established GMF for SAR frequency and polarization, as retrieval will not be possible if the frequency and polarization of the SAR are not the same as that of the GMF. Specialized GMFs were developed under specified terms. The GMFs of CMOD4, CMOD5, and CMOD5.N, for instance, are all only applicable for VV-polarized SARs at C-band. For HH-polarized SARs, a polarization ratio has to be applied to convert their NRCSs to those at VV polarization [17], [18].

However, theoretical backscattering models based on electromagnetic wave's backscatter theory can simulate radar backscattering from oceanic surfaces at any microwave frequency and polarization [19]–[28]. These theoretical backscattering models can be used in the application of sea surface wind retrieval from SAR images [18], [27].

Microwave backscattering from a rough sea surface can be described by a composite Bragg scattering (CBS) model, which combines a two-scale backscatter model and a geometric optics model [24]–[27]. In the CBS model, a small local incidence angle setting should be given to simulate the NRCS from the sea surface. The NRCS in the local incidence angle which is smaller than this given setting value should be calculated by geometric optics solution for specular reflection instead of the two-scale backscattering solution. However, this setting is not the same in all investigations, e.g., it was 18° in [26], while it was 10° in [27].

This study aimed to find an optimized small incidence angle setting by comparing the NRCS of the CBS model with Canadian RADARSAT-2 (R2) satellite SAR images. Furthermore, sea surface wind speeds are retrieved from SAR images of both R2 at C-band and CSK at X-band using the CBS model with the optimized small incidence angle setting. In this article, Section II introduces the SAR, scatterometer and buoy data, which were

Manuscript received December 11, 2019; revised February 4, 2020; accepted February 11, 2020. Date of publication March 23, 2020; date of current version April 16, 2020. This work was supported in part by the National Natural Science Foundation of China under Grants 41876211, 41506206, 41876204, and 41476152 and in part by the National Key Research and Development Program of China under Grant of 2016YFC1401000. *(Corresponding author: Mingsen Lin.)*

The authors are with the National Satellite Ocean Application Service, Key Laboratory of Space Ocean Remote Sensing and Application,Ministry of Natural Resources, Beijing 100081, China (e-mail: yexiaomin2011@foxmail.com; mslin@mail.nsoas.org.cn; qsong@mail.nsoas.org.cn; qmwang@mail.nsoas.org.cn).

Digital Object Identifier 10.1109/JSTARS.2020.2974660

used in this study; the CBS model; the methods of finding its optimized small incidence angle setting and the sea surface wind speed retrieval from SAR images. Section III details the results of the optimized small incidence angle setting, the sea surface wind speed retrieval from the SAR images and the evaluation of these retrievals by nearly simultaneous wind speeds of the Advanced Scatterometer (ASCAT) onboard European Metop-A/B satellites. Section IV concludes this article.

II. Data and Methodology

A. Data

1) SAR Images: Spaceborne SAR images at both the C-band (5.405 GHz) and X-band (9.6 GHz) are used in this study. The C-band SAR images were taken by Canadian RADARSAT-2 satellite (R2), an Earth observation satellite launched on December 14, 2007. R2 carries a single sensor C-band SAR with HH, HV, VV, and VH polarization modes and multiple scanning modes [29]. The R2 SAR images used in this study are acquired by ScanSAR wide-beam mode with a swath width of 500 km, a spatial resolution of 100 m and incidences ranging from 19° to 49°.

The X-band SAR images were taken by CSK, which is an Earth observation satellite system funded by the Italian Ministry of Research and Ministry of Defence and conducted by the Italian Space Agency. The CSK system includes four identical medium-sized satellites equipped with SAR sensors at the X-band with global coverage of the Earth. The CSK SAR images used in this study are acquired by ScanSAR HugeRegion mode with a swath width of 200 km and a spatial resolution of 100 m. Two CSK SAR images are used in this study for sea surface wind speed retrieval from the X-band SAR images.

A total of 98 C-band R2 SAR images are used in this study. A total of 52 of them are used to find the optimized small incidence angle setting for the CBS model, and the remaining 46 are used to retrieve coastal sea surface wind speeds. The X-band CSK SAR images, limited by data availability, are only used for wind speed retrieval tests. The R2 SAR images used for the optimized small incidence angle setting determined from the CBS model and CSK SAR images both cover the northern South China Sea (SCS), while those used for sea surface wind speed retrieval cover the northern SCS and the Bohai Sea of China.

2) Sea Surface Wind Data From a Space-Borne Microwave Scatterometer and Buoys: Wind speeds and directions both from microwave scatterometer remote sensing products and obtained measurements from mooring buoys are used in this study to evaluate the CBS model and the results of wind speed retrieval from SAR.

ASCAT, the microwave scatterometer used in this study, is a C-band (5.255 GHz) scatterometer carried onboard the European organization for the exploitation of meteorological satellites (EUMETSAT) Metop-A and Metop-B satellites. The Metop-A satellite was launched on October 19, 2006. It became fully operational in mid-May 2007 and continues to operate today. Metop-B was launched on September 17, 2012. Both ASCATs onboard Metop-A and Metop-B are identical instruments. The main objective of ASCAT is to measure wind speeds and directions over global oceans. The operational wind speed and direction products of ASCAT with a resolution of 25 km and a swath of 500 km used in this study are provided by the ocean satellite data exchange between EUMETSAT and National Satellite Ocean Application Service (NSOAS), China. The wind directions are used as the external sources of the wind speed retrieval model, while the sea surface wind speeds are used to validate the wind speed retrieved.

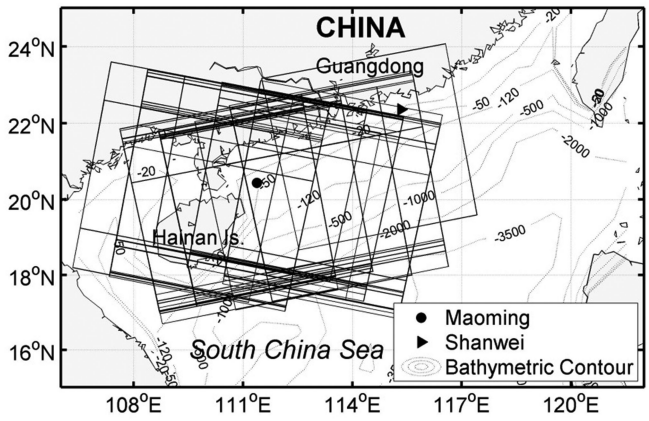

Fig. 1. Locations of the meteorological buoys and bathymetric contours of the northern South China (unit of water depth: m), where the boxes shown in the figure indicate the coverage areas of the R2 SAR images used for this CBS model study.

The meteorological mooring buoys used in this study are located in the coastal areas of Maoming (buoy no. 59765) and Shanwei (buoy no. 59506), with water depths of 50- and 20-m and offshore distances of 100- and 20-km, respectively. Maoming and Shanwei are cities of Guangdong Province, China. These meteorological mooring buoy data are provided by the Guangzhou meteorological observatory, China, and their locations and bathymetric contours of the northern SCS are shown in Fig. 1. The sea surface wind speeds and directions of the buoys are measured at a height of 10-m above the sea surface and reported once every 20 min. In Fig. 1, the coverage areas of the 52 SAR images used for finding the optimized small incidence angle setting of the CBS model are also shown.

B. Methodology

1) CBS Model: Microwave backscattering from the rough sea surface can be simulated by a CBS theoretical model, which is a combination of the two-scale backscatter model and a geometric optics model. The two-scale backscatter theory is described by electromagnetic Bragg backscattering from short ocean surface waves, which are tilted by long waves and of which the wavelengths are comparable to the incident electromagnetic wave [24]–[27]. The solution of the NRCS (i.e., backscattering coefficient) for Bragg scattering is

$$\sigma_{pq}^{0} = 16\pi k^4 \cos^4\theta |g_{pq}(\theta)|^2 W(2k\sin\theta, \varphi) \qquad (1)$$

where k is the radar wavenumber, θ is the incidence angle, and W is the wavenumber spectrum of the ocean surface. The wave spectrum of the ocean surface, developed by [30], is used in this

study. φ is the wave direction relative to the wind, $2k\sin\theta$ is the surface wavenumber of the Bragg resonance component, and the subscripts p and q denote polarization and can apply to V or H. For copolarization, g_{pp} is defined as

$$g_{HH}(\theta) = \frac{\varepsilon_r - 1}{\left[\cos\theta + \sqrt{\varepsilon_r - \sin^2\theta}\right]^2} \tag{2}$$

$$g_{VV}(\theta) = \frac{(\varepsilon_r - 1)\left[\varepsilon_r\left(1 + \sin^2\theta\right) - \sin^2\theta\right]}{\left[\varepsilon_r\cos\theta + \sqrt{\varepsilon_r - \sin^2\theta}\right]^2} \tag{3}$$

where ε_r is the relative dielectric constant of seawater [31]. For a slightly rough patch tilted by the ocean surface, the solutions of the NRCS are as follows [26], [27]:

$$\sigma_{0VV} = 16\pi k^4\cos^4\theta_i \left|g_{VV}(\theta_i)\left(\frac{\alpha\cos\delta}{\alpha_i}\right) + g_{HH}(\theta_i)\left(\frac{\sin\delta}{\alpha_i}\right)\right|^2 W(K_{Bx}, K_{By}) \tag{4}$$

$$\sigma_{0HH} = 16\pi k^4\cos^4\theta_i \left|g_{HH}(\theta_i)\left(\frac{\alpha\cos\delta}{\alpha_i}\right) + g_{VV}(\theta_i)\left(\frac{\sin\delta}{\alpha_i}\right)\right|^2 W(K_{Bx}, K_{By}) \tag{5}$$

where $K_{Bx} = 2k\alpha$ and $K_{By} = 2k\gamma\sin\delta$ are the two wavenumber components of the Bragg resonance waves; the x–z plane is the plane of incidence; y is perpendicular to the x–z plane; $\theta_i = \cos^{-1}[\cos(\theta + \psi)\cos\delta]$ is the local incidence angle; $\alpha_i = \sin\theta_i$; $\alpha = \sin(\theta + \psi)$; $\gamma = \cos(\theta + \psi)$; and ψ and δ are the angles of the tilting surface parallel and perpendicular to the radar incidence plane, respectively. Accounting for all ocean surfaces titled through the probability density function (PDF) of the ocean surface slopes, the NRCS of the ocean surface is

$$\sigma_{0pp}(\theta) = \int_{-\infty}^{\infty}\int_{-\cot\theta}^{\infty}\sigma_{0pp}(\theta i)P\theta(Zx', Zy')\,dZx dZy \tag{6}$$

$$P_\theta(Zx', Zy') = (1 + Zx\tan\theta)\,P(Zx', Zy') \tag{7}$$

where Zx', Zy',Zx, and Zy are the surface slopes in the directions of x', y', x, and y, respectively; $Zx = \tan\psi$, $Zy = \tan\delta$, x' is in the wind direction, and y' is perpendicular to the wind direction. $P(Zx', Zy')$ is the PDF of large-scale waves as viewed at an incident angle θ in the coordinates of $x' - y' - z$, and the relations among Zx, Zy, Zx', and Zy' are

$$Zx' = Zx\cos\phi + Zy\sin\phi \tag{8}$$

$$Zy' = Zy\cos\phi - Zx\sin\phi \tag{9}$$

where ϕ is the angle between x and x'. In this study, we chose the PDF of the ocean surface made by [32], which was also chosen by [27] and reported that

$$P(Zx', Zy') = \frac{1}{2\pi\sigma_u\sigma_c}\exp\left(-\frac{Zx'^2}{2\sigma_u^2} - \frac{Zy'^2}{2\sigma_c^2}\right) \cdot\left[1 - \frac{C_{21}}{2}\left(\frac{Zy'^2}{\sigma_c^2} - 1\right)\frac{Zx'}{\sigma_u} - \frac{C_{03}}{6}\left(\frac{Zx'^3}{\sigma_u^3} - \frac{3Zx'}{\sigma_u}\right)\right.$$

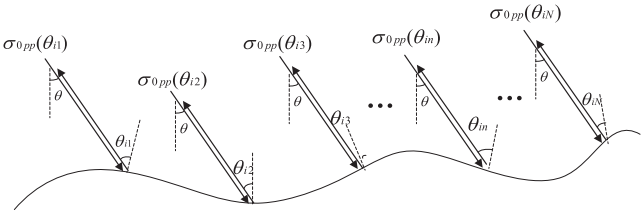

Fig. 2. Schematic sketch of the geometry of radar wave backscattering from sea surface.

$$\left. + \frac{C_{40}}{24}\left(\frac{Zy'^4}{\sigma_c^4} - 6\frac{Zy'^2}{\sigma_c^2} + 3\right) + \frac{C_{22}}{4}\left(\frac{Zy'^2}{\sigma_c^2} - 1\right) \times\left(\frac{Zx'^2}{\sigma_u^2} - 1\right) + \frac{C_{04}}{24}\left(\frac{Zx'^4}{\sigma_u^4} - 6\frac{Zx'^2}{\sigma_u^2} + 3\right)\right] \tag{10}$$

where $C_{40} = 0.4$, $C_{22} = 0.1$, $C_{04} = 0.2$, $C_{21} = -0.11U_{10}/14$, $C_{03} = -0.42U_{10}/14$, σ_u^2, and σ_c^2 are the upwind and crosswind mean square slopes of the ocean surface roughness. $\sigma_u^2 = 0.005 + 0.78\times10^{-3}U_{12.5}$, $\sigma_c^2 = 0.003 + 0.84\times10^{-3}U_{12.5}$ and U_{10} and $U_{12.5}$ are the wind speeds at elevations of 10 and 12.5 m above sea surface, respectively. The relation between sea surface wind speed and the wind speed at a given elevation is [33]

$$\frac{U_z}{U_{10}} = \frac{\ln\left(\frac{z}{0.0016}\right)}{8.7403}. \tag{11}$$

For a small local incidence angle (less than 18° in [26], while 10° in [27]), the geometric optics solution for specular reflection is used to replace the two-scale backscattering solution of (4) or (5). The geometric optics solution is

$$\sigma_{0GO}(\theta_i) = \frac{|R(0)|^2}{2\sigma_u^2\sigma_c^2}\sec^4\theta_i\exp\left(\frac{-\tan^2\theta_i}{2\sigma_u^2}\right) \tag{12}$$

where σ_u^2 and σ_c^2 are the filtered upwind and crosswind mean square slopes of the ocean surface roughness, respectively. The Fresnel reflection coefficient for normal incidence, which is identical for HH and VV polarizations, is

$$|R(0)|^2 = \frac{\left|1 - 2\sqrt{\varepsilon_r} + \varepsilon_r\right|}{\left|1 + 2\sqrt{\varepsilon_r} + \varepsilon_r\right|} \tag{13}$$

where ε_r is the relative dielectric constant of seawater.

The CBS model is built by combining formulas (2) to (13). The NRCS of microwaves from the ocean surface can be calculated by using this radar backscattering theoretical model by formula (6) [i.e., the CBS model of formulas (2) to (13)] with given radar incidence, azimuth angle, and sea surface wind speed and direction. Sea surface wind speeds can also be reversed from the NRCS with the given wind directions, radar incidences, and azimuth angles by using the CBS model.

2) Comparison of the CBS Model With SAR Measurements: As mentioned in the above section, the NRCS from the sea surface can be calculated by the CBS model of formula (6), while formula (4) or (5) should be replaced by (12) when the local incidence angle of the radar wave is less than a threshold value of an angle. Fig. 2 shows the schematic sketch of the

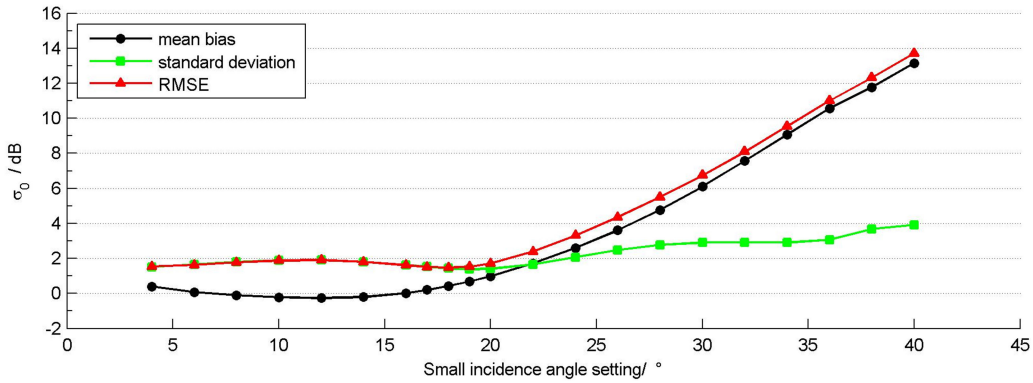

Fig. 3. Comparison of NRCSs of SAR images with CBS model at different small incidence angle setting.

geometry of radar wave backscattering from sea surface. θ is the incidence of radar wave; θ_{i1}, θ_{i2}, $\theta_{\rm in}$, and θ_{iN} are the local incidence angles which can be calculated by (4), (5), and (12). Then, the NRCS from sea surface by formula (6) can be rewritten by

$$\sigma_{0pp}(\theta) = \sum_{n=1}^{N} \sigma_{0pp} \cdot P_\theta(\theta_{\rm in}) \tag{14}$$

$$\sigma_{0pp} = \begin{cases} \sigma_{0pp}\left(\theta_{\rm in}\right) & \text{if } \theta_{\rm in} > \theta_m \\ \sigma_{0GO}\left(\theta_{\rm in}\right) & \text{if } \theta_{\rm in} \le \theta_m \end{cases} \tag{15}$$

where $P_\theta(\theta_{\rm in})$ is the PDF of the sea surface slopes described by (7); $\sigma_{0pp}(\theta_{\rm in})$ is the backscattering coefficient described by (4) and (5), while $\sigma_{0GO}(\theta_{\rm in})$ is described by (12). The threshold value of the local incidence angle θ_m is called the small incidence angle setting for the CBS model.

To find the value of optimized small incidence angle setting θ_m, the simultaneously obtained measurements from buoys are collocated with R2 SAR observations. The buoy measurements and the R2 observations are paired with a spatial separation of less than 10 km between the centers of the R2 images and buoy locations and a time interval of less than or equal to 30 min, which is the same criteria as in [27]. We calculate the NRCSs by the CBS model under the conditions of sea wind speed and the directions of buoy measurements and radar geometry (i.e., incidence and azimuth angles). Then, we compared the NRCSs of SAR images with the CBS model at different small incidence angle settings θ_m, which is assumed to be a value ranging from 4° to 40° with a step of 2°.

3) Sea Surface Wind Retrieval by the CBS Model: Both the CBS model and GMF can be used to simulate the NRCS of radar waves from sea surfaces under given sea state and radar geometry conditions. We can also use these CBS models and GMFs to retrieve sea surface wind speeds from the NRCS in a given wind direction and radar geometry.

The wind directions used for wind retrieval from SAR images came from satellite scatterometers, *in situ* measurements, operational meteorological model outputs or the wind directions from the featured SAR image [6], [8], [34]–[36]. We retrieve the sea surface wind speed from the SAR image (both R2 SAR at C-band and CSK SAR at X-band) using the CBS model by using the wind directions of nearly simultaneous ASCAT measurements as the input of the model in this study. To evaluate the results, we retrieved the wind speed by the GMF of CMOD5.N for the same R2 SAR images.

III. Results and Analysis

A. Optimized Small Incidence Angle Setting of the CBS Model

After matching the SAR images and buoy measurements, we obtain 52 collocated data points (i.e., 52 NRCSs of raw SAR images and CBS model with simultaneous sea surface wind measured by buoys) with 51 matching SAR images in VV polarization. The 52 buoy wind speeds range from 2.5 to 14.2 m/s, with an average value of 7.1 m/s and a standard deviation of 2.9 m/s. We calculated the mean bias, standard deviation of the biases, and root mean square error (RMSE) of these 52 collocated NRCSs at different small incidence angles, and the results are shown in Fig. 3. We find that the RMSE and standard deviation reach a minimum from 16° to 20°. To obtain the optimized small incidence angle setting, we recalculate the NRCSs by the CBS model at a small incidence angle setting from 16° to 20° with a step of 1°.

As shown in Fig. 3, we can see that the RMSEs of the NRCSs change slowly, ranging from 1.48 to 1.90 dB, and the biases and standard deviations are also not greater than 2 dB at a small incidence angle setting from 4° to 20°. Both the RMSE and mean bias increase quickly with the increase in the small incidence angle setting when they are greater than 20°, and the RMSE is 2.38 dB at a small incidence angle of 22°. From the results shown in Fig. 3, we can conclude that the small incidence angle setting must be no greater than 20°, and the RMSE and mean bias reach their smallest values at the small incidence angle setting of 18°. This indicates that the optimized small incidence angle setting of the CBS model is 18° for the microwave frequency of the C-band at sea surface wind speeds ranging from 2.5 to 14.2 m/s (i.e., the wind speed range measured by buoys used in this study). The optimized small incidence angle setting concluded from this study is the same as that selected by [26].

Fig. 4(a) shows the scatter plot of the NRCSs of the SAR images and the CBS model at a small incidence angle setting

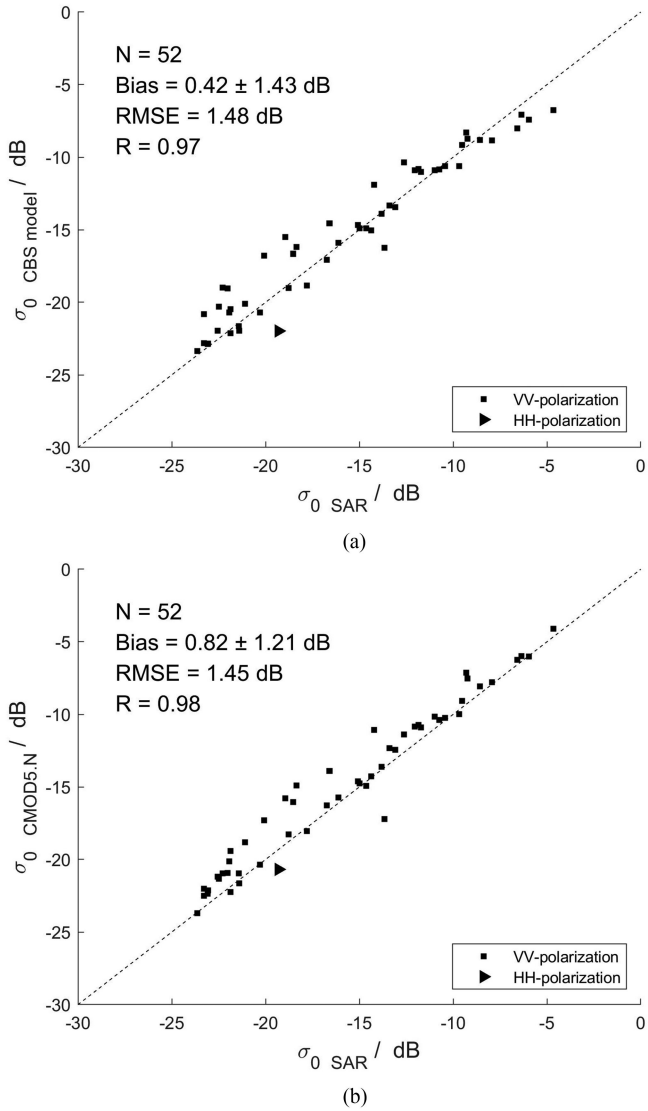

Fig. 4. Comparison of the NRCSs from SAR images and the model calculations under simultaneous sea surface wind speeds and directions measured by buoys. (a) The CBS model at the optimized small incidence angle setting of 18°. (b) CMOD5.N.

of 18°. The bias of these 52 collocated data is 0.42 ± 1.43 dB, the RMSE is 1.48 dB, and the linear correlation coefficient (i.e., *R* shown in Fig. 4) is 0.97. To compare the CBS model with the GMF of CMOD5. N, we perform the same comparison as introduced in Section II with CMOD5.N instead of the CBS model. For the SAR images in HH polarization, we use the polarization ratio function to calculate the NRCS by CMOD5.N [17]. The calculation equation and the polarization ratio function R_p are

$$\sigma_{0\,HH}(\mathrm{CMOD5.N}) = R_p \cdot \sigma_{0\,VV}\ (\mathrm{CMOD5.N}) \tag{16}$$

$$Rp = \left(1 + 0.6\tan^2\theta\right)^2 / \left(1 + 0.6\tan^2\theta\right)^2 \tag{17}$$

where $\sigma_{0\,VV}\ (\mathrm{CMOD5.N})$ is the NRCS calculated by CMOD5.N, and θ is the radar incidence.

A comparison of the NRCSs from the SAR images and CMOD5.N is shown in Fig. 4(b) with a bias of 0.82 ± 1.21 dB, RMSE of 1.45 dB, and *R* of 0.98.

From the comparison results shown in Fig. 4, we can see that the NRCS calculated by the CBS model at the C-band has almost the same accuracy as that of CMOD5.N with the same SAR observation geometry and sea surface wind speed.

In this study, the optimized small incidence angle setting of the CBS model is found by comparing the NRCS of R2 SAR images with the CBS model. Its confidence level depends on the amount of data used and the sea sate distributions. Fifty-two collocated data with wind speeds ranging from 2.5 to 14.2 m/s and an average value of 7.1 m/s are used in this study. There are no data with wind speeds higher than 15 m/s. Furthermore, only one collocation SAR image with HH polarization is used. These results indicate that the optimized small incidence angle setting of 18° in this study is relatively more reliable for the CBS model at the C-band with VV polarization at low or moderate wind speeds (no higher than 14 m/s). In high sea states, microwave scattering from the sea surface can be significantly affected by other scattering sources, such as rainfall, wave breaking and white caps [37], [38], and the CBS model should be further studied and improved.

For the sea surface wind speed ranging from 2.5 to 14.2 m/s used in this study, the comparison of NRCSs calculated by the theoretical CBS model with the optimized small incidence angle and CMOD5.N at C-band with a relative wind direction is 0° and a radar incidence of 34°, which are the average radar incidence of R2 SAR in ScanSAR wide-beam mode, is shown in Fig. 5(a). It is noted that this radar incidence is the angle of radar geometry, i.e., the θ in formulas (6) and (7), which is not the same parameter as the optimized small incidence angle setting. Fig. 5(b) is the comparison of NRCSs calculated by the theoretical CBS model with the optimized small incidence angle and CMOD5.N at C-band with a radar incidence of 34° and a sea surface wind speed of 7.1 m/s, which is the average value of the collocated wind speeds used in this study. From Fig. 5(a) and (b), we can see that the NRCSs calculated by CBS model at C-band with the optimized small incidence angle found in this study are very close to that of CMOD5.N, the maximal difference is no greater than 1.5 dB, which is the same order of magnitude as the RMSE shown in Fig. 4.

B. Sea Surface Wind Speed Retrieval Results From SAR Images by the CBS Model

As mentioned in the above section, the CBS model has almost the same accuracy as CMOD5.N in microwave backscattering from sea surface simulation at C-band. We use the nearly simultaneous (less than 3 h) wind directions offered by the ASCAT scatterometer as the input of the CBS model; then, the sea surface wind speeds are retrieved from the NRCSs of SAR images. We retrieved sea surface wind speed from both C- and X-band SAR images by the CBS model with the small incidence angle setting of 18° found in this study.

1) Results From the R2 SAR Images at the C-Band: A total of 32 R2 SAR images used in sea surface wind speed retrieval in this study cover the northern SCS, and the remaining 14 cover the

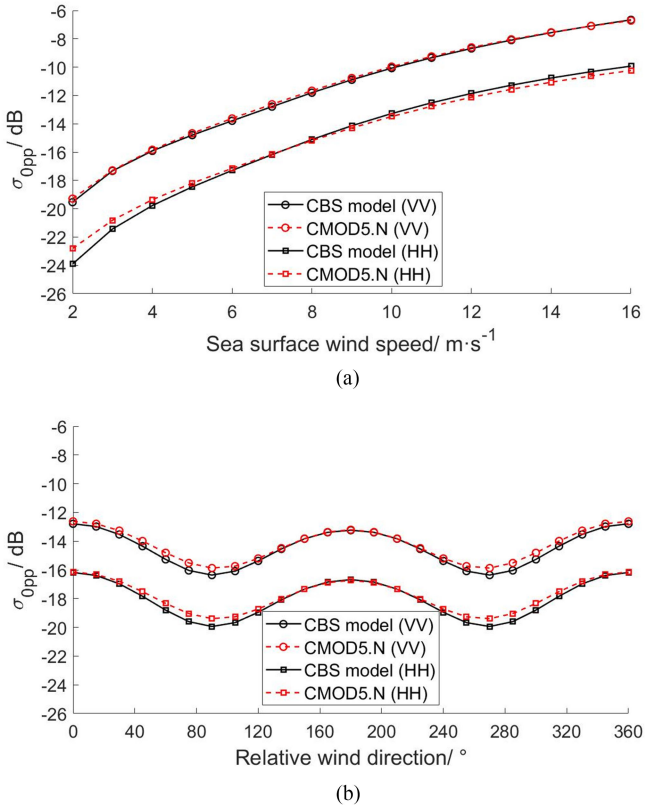

Fig. 5. Comparison of the NRCSs from CBS model at the optimized small incidence angle setting of 18° and CMOD5.N. (a) The radar incidence is 34° and the relative wind direction is 0°. (b) The radar incidence is 34° and the sea surface wind speed is 7.1 m/s.

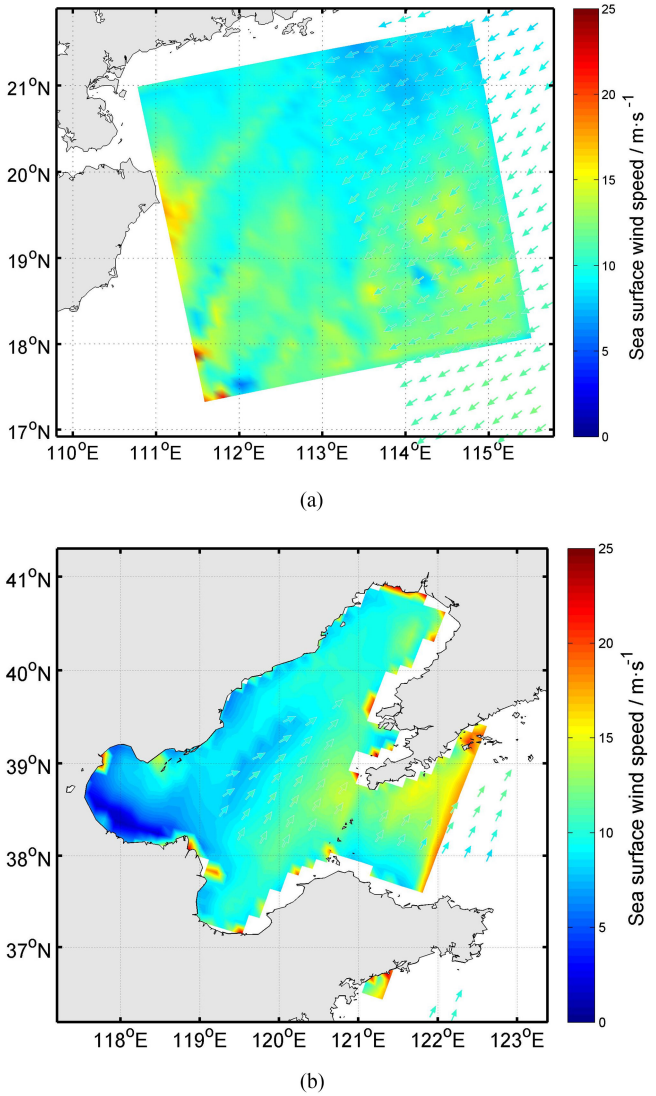

Fig. 6. Sea surface wind speeds retrieved from R2 SAR images at C-band by the CBS model. (a) VV polarization acquired at 10:37 UTC on Jan. 16, 2014. (b) HH polarization acquired at 22:56 UTC on Dec. 18, 2014. The color-coded arrows represent the nearly simultaneous sea surface vectors of ASCAT.

Bohai Sea of China. A total of 42 images are in VV polarization, and the remaining four are in HH polarization. The sea surface wind speed retrieval from SAR images is validated against the nearly simultaneous ASCAT observations. Fig. 6 shows these two cases of sea surface wind speeds retrieved from R2 SAR images in VV and HH polarization. In the figure, the color-coded arrows represent the nearly simultaneous sea surface vectors of ASCAT, and the background represents the wind speed from the SAR image. Their indistinguishable colors indicate that there are small differences in wind speeds between SAR and its nearly simultaneous ASCAT. Fig. 7(a) and (b) shows the scatterplot of the comparison of sea surface wind speeds of the all 46 SAR images and the simultaneous ASCAT.

From Fig. 7, we can see the RMSE of all the sea surface wind speeds from the 42 SAR images in VV polarization is 1.5 m/s, while the value is 1.7 m/s for the remaining 4 SAR images in HH polarization. To compare the CBS model with the GMF of CMOD5.N, we also repeat the sea wind speed retrieval process from R2 SAR images by CMOD5.N instead of the CBS model. The RMSE of all the sea surface wind speeds from the 42 SAR images in VV polarization by CMOD5.N is 1.2 m/s, while the value is 1.7 m/s for the remaining 4 SAR images in HH polarization by CMOD5.N. The accuracy evaluations of these retrieved wind speeds are detailed in Table I. The variable *N* in the table is the wind speed number for the comparison between SAR and ASCAT in one SAR image; the detection time difference represents the time difference from SAR observation time to ASCAT. The spatial resolution of the compared wind speed retrieved from SAR is the same as ASCAT (25 km). In general, we can retrieve sea surface wind speeds from SAR images at a high spatial resolution (e.g., hundreds of meters). We use the retrieval wind speed with a resolution of 25 km in this study to match the sea surface wind vectors of ASCAT for validation. It is noted that the wind speed numbers (*N*) for comparison between SAR-derived wind speed from CMOD5.N and CBS model and ASCAT are not the same in some cases in Table I, this is because some abnormal data points of which the biases are greater than three times of their standard deviation are eliminated by pauta criterion. The number of eliminated abnormal data points is no more than three.

From Table I, we can see that 38 of 46 (the percentage is approximately 83%) RMSEs by the CBS model are smaller than 2.0 m/s. This indicates that most of the sea surface wind retrieval

TABLE I
ACCURACY EVALUATION RESULTS OF THE SEA SURFACE WIND SPEED RETRIEVAL FROM R2 SAR IMAGES

No.	Time (UTC)	Sea Area	Polarization	Satellite of ASCAT	Detection time difference (h)	Results by CMOD5.N			Results by CBS model			Average wind speed of ASCAT (m/s)
						N	Mean bias±std (m/s)	RMSE (m/s)	N	Mean bias±std (m/s)	RMSE (m/s)	
1	2014/01/16 10:37	northern SCS	VV	Metop-B	2.6	127	0.2±0.6	0.7	127	0.3±0.9	0.9	10.3±1.2
2	2014/01/21 09:56	Bohai Sea	HH	Metop-A	2.4	43	-0.7±1.9	2.0	43	0.4±1.8	1.8	8.4±1.0
3	2014/01/23 10:33	northern SCS	VV	Metop-A	2.7	250	-0.2±0.7	0.7	252	-0.1±0.8	0.8	8.7±1.2
4	2014/01/18 09:41	northern SCS	VV	Metop-B	2.8	14	-0.5±0.5	0.6	14	-1.5±0.7	1.6	12.8±0.3
5	2014/02/11 09:41	northern SCS	VV	Metop-B	2.9	16	-0.3±1.1	1.1	16	-0.2±1.8	1.8	12.3±0.5
6	2014/02/16 10:33	northern SCS	VV	Metop-A	2.7	244	0.0±0.7	0.7	244	0.3±0.7	0.8	4.1±1.8
7	2014/02/26 10:41	northern SCS	VV	Metop-A	2.5	51	-0.6±1.1	1.2	51	-0.6±1.1	1.2	4.3±0.6
8	2014/02/23 10:29	northern SCS	VV	Metop-B	2.9	91	-0.3±0.8	0.9	89	0.4±0.7	0.8	8.4±0.5
9	2014/03/17 09:50	northern SCS	VV	Metop-B	2.7	17	-0.4±0.5	0.6	17	-0.7±0.5	0.9	5.9±0.3
10	2014/03/12 10:33	northern SCS	VV	Metop-A	2.8	224	-0.0±0.9	0.9	223	0.2±0.9	0.9	2.7±1.3
11	2014/03/24 09:48	Bohai Sea	HH	Metop-A	2.8	22	-1.2±1.0	1.5	22	-1.6±1.2	2.0	4.8±1.2
12	2014/04/5 10:33	northern SCS	VV	Metop-A	2.8	154	-0.7±0.9	1.2	154	-0.3±0.7	0.7	8.4±0.8
13	2014/04/8 10:45	northern SCS	VV	Metop-B	2.5	37	0.1±1.2	1.2	37	0.2±1.2	1.2	3.9±2.7
14	2014/04/15 10:41	northern SCS	VV	Metop-A	2.6	158	-0.2±0.6	0.6	159	-0.0±0.6	0.6	8.0±0.7
15	2014/04/29 10:33	northern SCS	VV	Metop-A	2.9	106	-0.8±0.4	0.9	104	-0.1±0.4	0.4	6.0±0.9
16	2014/04/27 09:56	Bohai Sea	VV	Metop-A	2.6	54	1.1±0.9	1.4	54	1.3±0.9	1.6	5.3±2.5
17	2014/04/03 09:56	Bohai Sea	VV	Metop-A	2.5	81	-1.0±2.1	2.3	81	-1.6±2.4	2.9	8.2±2.9
18	2014/04/10 09:52	Bohai Sea	VV	Metop-B	2.8	50	0.0±1.3	1.3	50	0.3±1.5	1.5	3.0±1.3
19	2014/05/09 10:41	northern SCS	VV	Metop-A	2.6	193	-1.6±1.8	2.4	193	-2.1±2.1	3.0	8.5±2.0
20	2014/05/16 10:37	northern SCS	VV	Metop-B	2.9	173	-1.3±0.7	1.5	173	-0.6±0.8	0.9	6.0±0.5
21	2014/05/23 10:33	northern SCS	VV	Metop-A	2.9	61	-1.1±0.5	1.2	62	0.2±0.6	0.6	6.7±0.4
22	2014/05/02 10:45	northern SCS	VV	Metop-B	2.5	85	-0.5±1.6	1.6	85	-0.2±1.6	1.6	7.4±2.7
23	2014/05/04 09:52	Bohai Sea	VV	Metop-B	2.8	29	-0.1±2.2	2.2	29	0.3±2.4	2.4	4.0±0.8
24	2014/05/21 09:56	Bohai Sea	VV	Metop-A	2.7	38	-0.1±0.9	0.9	38	0.2±0.7	0.8	4.6±0.6
25	2014/05/26 10:45	northern SCS	VV	Metop-B	2.6	113	-0.7±0.7	1.0	113	-1.1±0.8	1.4	3.7±0.8
26	2014/06/09 10:37	northern SCS	VV	Metop-B	2.9	111	-0.6±1.1	1.2	111	-0.0±1.3	1.3	3.7±1.5
27	2014/06/19 10:45	northern SCS	VV	Metop-B	2.7	124	-1.3±0.8	1.6	126	-2.3±1.5	2.7	6.9±0.6
28	2014/06/26 10:41	northern SCS	VV	Metop-A	2.8	200	-0.6±0.7	0.9	199	-0.5±0.7	0.8	4.9±0.7
29	2014/06/14 09:56	Bohai Sea	VV	Metop-A	2.7	34	-1.4±0.7	1.5	34	-1.4±0.8	1.6	3.0±1.1
30	2014/07/10 22:52	Bohai Sea	VV	Metop-B	2.4	28	-1.7±0.9	1.9	28	-1.6±0.9	1.8	9.2±1.6
31	2014/07/17 22:48	Bohai Sea	VV	Metop-A	2.5	76	0.1±1.2	1.2	77	0.2±1.2	1.2	3.5±1.1
32	2014/07/13 10:45	northern SCS	VV	Metop-B	2.7	142	-0.1±0.8	0.8	143	-0.3±0.7	0.7	5.7±1.0
33	2014/07/20 10:41	northern SCS	VV	Metop-A	2.8	142	-0.5±0.7	0.9	141	-0.1±0.7	0.7	3.9±0.8
34	2014/07/25 10:00	Bohai Sea	VV	Metop-B	2.7	22	0.9±1.6	1.8	22	0.8±1.4	1.5	6.0±1.4
35	2014/08/01 09:56	Bohai Sea	VV	Metop-A	2.8	4	-0.4±0.1	0.4	4	0.4±0.1	0.4	5.0±0.4
36	2014/08/06 10:45	northern SCS	VV	Metop-B	2.8	146	-0.3±1.2	1.2	148	-1.1±1.3	1.7	5.0±1.3
37	2014/08/13 10:41	northern SCS	VV	Metop-A	2.9	92	-0.5±0.9	1.0	92	-0.1±1.3	1.3	5.8±1.5
38	2014/09/30 10:41	northern SCS	VV	Metop-A	3.0	10	-2.1±1.1	2.3	10	-2.0±0.9	2.2	4.5±0.3
39	2014/08/30 10:45	northern SCS	VV	Metop-B	2.8	110	-0.8±1.2	1.4	110	-0.4±1.2	1.3	5.4±0.6
40	2014/10/17 10:45	northern SCS	VV	Metop-B	2.9	21	-0.9±0.9	1.2	19	0.2±1.0	1.0	9.8±0.7
41	2014/11/07 10:33	northern SCS	VV	Metop-B	2.6	132	0.2±0.8	0.8	134	0.6±1.2	1.4	9.1±1.5
42	2014/12/01 10:33	northern SCS	VV	Metop-B	2.6	188	-0.2±1.0	1.0	187	0.8±1.7	1.9	13.0±0.8
43	2014/12/18 10:37	northern SCS	VV	Metop-A	2.5	60	-0.1±0.8	0.8	60	2.0±1.4	2.4	13.0±0.5
44	2014/12/25 10:33	northern SCS	VV	Metop-B	2.7	238	-0.3±0.9	0.9	237	1.4±1.5	2.0	12.8±1.0
45	2014/12/18 22:56	Bohai Sea	HH	Metop-A	2.6	38	0.9±0.9	1.3	37	-0.6±0.9	1.1	10.9±0.9
46	2014/12/25 22:52	Bohai Sea	HH	Metop-B	2.8	31	-0.7±1.8	1.9	31	-0.5±2.0	2.0	3.9±1.2

results from R2 SAR images by the CBS model have a relatively high accuracy. The average value of the 46 RMSEs of sea surface wind speeds retrieved by the CBS model is 1.5 m/s, while the value is 1.2 m/s for CMOD5.N. The histogram distribution of RMSEs is shown in Fig. 8. The histogram boundaries range from 0 to 3 m/s with a step of 0.5 m/s. From Table I and Fig. 8, we can see that the RMSEs of the CBS model and CMOD5.N have small differences with a bias of 0.3 ± 0.4 m/s.

For RMSEs greater than 2 m/s, see the results of no. 17 and 19 in Table I. The cause may be due to the great change in wind direction, which is the input of the CBS model and CMOD5.N. As detailed in Table I, the acquired time differences in SAR and ASCAT are all equal to or greater than 2.4 h, between which the wind directions may largely change in some cases, such as in the nearby area of tropical cyclone. The sea surface wind speeds of ASCAT for validation range from 2.2 to 13.8 m/s. Moreover, considering that the wind speeds of buoys used to find the optimized small incidence angle in the above section of this study ranged from 2.5 to 14.2 m/s, sea surface wind speed retrieval by the CBS model with a small incidence angle setting of 18° is relatively reliable under sea surface wind speed conditions of no greater than 14 m/s.

2) Results From the CSK SAR Images at X-Band: Limited by the amount of SAR data, only two CSK SAR images were used in the sea surface wind speed retrieval test in this study. The two SAR images at the X-band both cover the northern SCS. The sea surface wind speeds retrieved from the CSK SAR images by the CBS model are shown in Fig. 9. The nearly simultaneous sea surface wind vectors of ASCAT are also shown; see the color-coded arrows. The acquired time differences between SAR and ASCAT for Fig. 9(a) and (b) are 2.8 and 2.5 h, respectively.

As shown in Fig. 9, most of the color-coded arrows are almost identical with the wind speed field background from the SAR images. This means that there are small differences between these two wind speeds. Due to the different coverage areas of the SAR image and ASCAT [as shown in Fig. 9(a)], we only calculate the average wind speed in the box shown in Fig. 9(a). The values are 6.3 and 6.6 m/s for SAR and ASCAT, respectively. For Fig. 9(b), the RMSE of the wind speeds from the SAR image against nearly simultaneous ASCAT vectors is 1.6 m/s. These

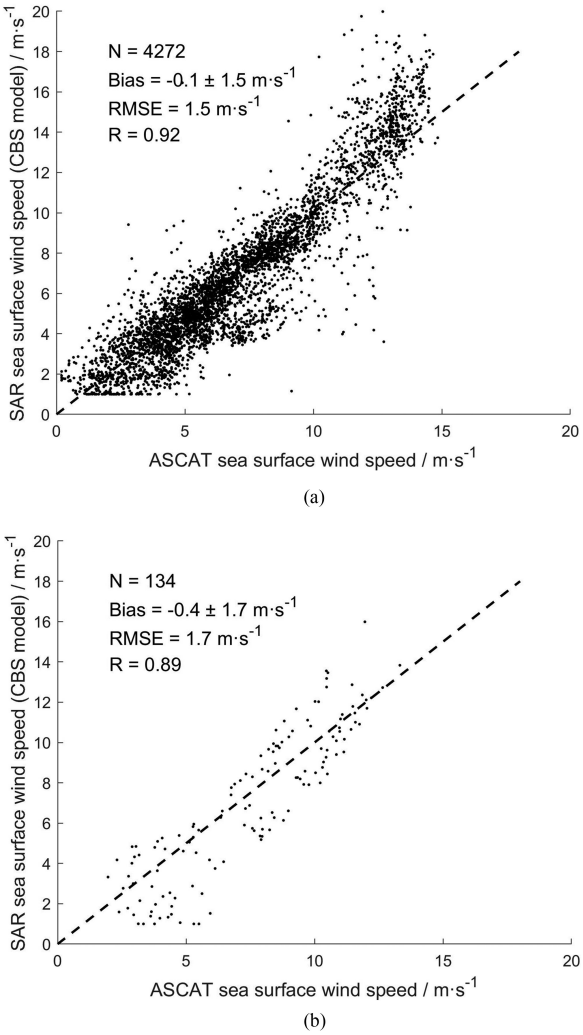

Fig. 7. Scatterplot of sea surface wind speeds retrieved from R2 SAR images at the C-band by the CBS model against nearly simultaneous ASCAT data. (a) 42 SAR images in VV polarization. (b) Four SAR images in HH polarization.

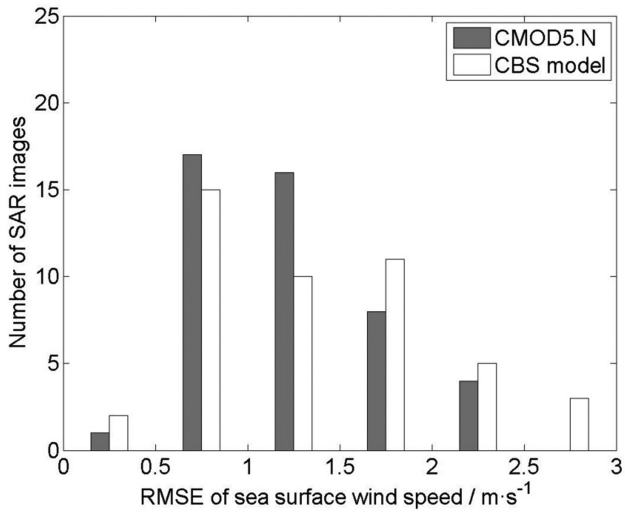

Fig. 8. Histogram distribution of the RMSEs of sea surface wind speeds retrieved from R2 SAR images by the CBS model and CMOD5 against nearly simultaneous measurements of ASCAT.

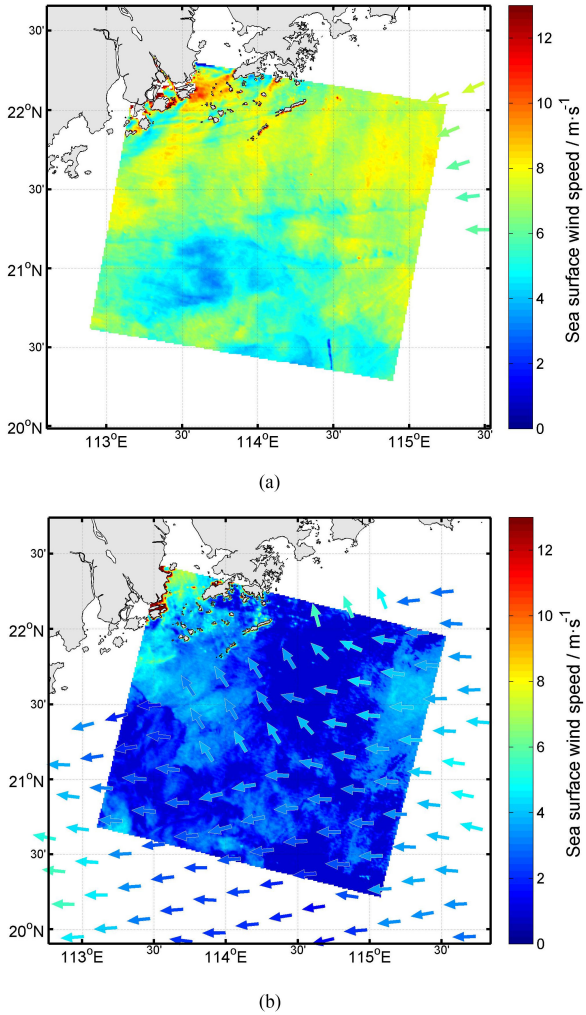

Fig. 9. Sea surface wind speeds retrieved from CSK SAR images at X-band in VV polarization by the CBS model. (a) Acquired at 10:09 UTC on April 28, 2013. (b) Acquired at 10:45 UTC on May 24, 2013. The color-coded arrows represent the nearly simultaneous sea surface vectors of ASCAT.

results indicate that the CBS model also works well in sea surface wind speed retrieval from X-band SAR images.

IV. Conclusion

The CBS model used in this study combines a two-scale backscatter model and a geometric optics model. For the small local incidence angle, the two-scale backscattering solution is replaced by a geometric optics solution for specular reflection. In this study, an optimized value of 18° of the small incidence angle setting is determined by comparing the NRCS between R2 SAR images and the CBS model with simultaneous sea surface wind measurements from meteorological mooring buoys in the northern SCS. The applications of sea surface wind speed retrieval from SAR images at both C-band from the Canadian R2 satellite and X-band from the Italian CSK satellite show that the CBS model with this optimized setting works well in surface wind speed retrieval from SAR images under the condition of low or moderate sea surface wind speeds (no higher than 14 m/s).

From case comparisons of the CBS model with R2 SAR images, it is believable that the optimized small incidence angle setting of 18° of the CBS model is suitable for the microwave frequency of the C-band with copolarization. More studies on the optimized small incidence angle setting of the CBS model and its application at other microwave frequencies cross polarizations or high sea states will be considered in future investigations.

ACKNOWLEDGMENT

The authors would like to thank Dr. F. Liao from the Guangzhou Meteorology Observatory, China, for providing the *In situ* measurements of sea surface wind from the meteorological mooring buoys.

REFERENCES

[1] A. Stoffelen and D. Anderson, "Scatterometer data interpretation: Estimation and validation of the transfer function CMOD4," *J. Geophys. Res.*, vol. 102, no. C3, pp. 5767–5780, Mar. 1997.

[2] Y. Quilfen, B. Chapron, T. Elfouhaily, K. Katsaros, and J. Tournadre, "Observation of tropical cyclones by high-resolution scatterometry," *J. Geophys. Res.*, vol. 103, no. C4, pp. 7767–7786, Apr. 1998.

[3] H. Hersbach, A. Stoffelen, and S. de Haan, "An improved C-band scatterometer ocean geophysical model function: CMOD5," *J. Geophys. Res.*, vol. 112, Mar. 2007, Art. no. C03006, doi:10.1029/2006JC003743.

[4] H. Hersbach, CMOD5.N: A C-band geophysical model function for equivalent neutral wind, ECMWF, Reading: U.K., Tech. Memo.554, Apr. 2008.

[5] A. Stoffelen, J. A. Verspeek, J. Vogelzang, and A. Verhoef, "The CMOD7 geophysical model function for ASCAT and ERS wind retrievals," *IEEE J. Sel. Topics Appl. Earth Observ. Remote Sens.*, vol. 10, no. 5, pp. 2123–2134, Apr. 2017.

[6] H. Lin, Q. Xu, and Q. Zheng, "An overview on SAR measurements of sea surface wind," *Prog. Nat. Sci., Mater.*, vol. 18, no. 8, pp. 913–919, Mar. 2008.

[7] D. R. Thompson, F. M. Monaldo, R. C. Beal, N. S. Winstead, W. G. Pichel, and P. Clemente-Colón's, "Combined estimates improve high-resolution coastal wind mapping," *EOS Trans. Amer. Geophys. Union*, vol. 82, no. 41, pp. 469–484, Jan. 2001.

[8] Q. Xu, H. Lin, Q. Zheng, P. Xiu, Y. Cheng, and Y. Liu, "Evaluation of ENVISAT SAR for sea surface wind retrieval in Hong Kong coastal waters of China," *Acta Oceanol. Sini.*, vol. 27, no. 4, pp. 57–62, Sep. 2008.

[9] B. Zhang, W. Perrie, J. Zhang, E. W. Uhlhorn, and Y. He, "High-resolution hurricane vector winds from C-band dual-polarization SAR observations," *J. Atmos. Ocean. Technol.*, vol. 31, no. 2, pp. 272–286, Jan. 2014.

[10] X. Li, "The first sentinel-1 SAR image of a typhoon," *Acta Oceanol. Sin.*, vol. 34, no. 1, pp. 1–2, Jan. 2015.

[11] A. Montuori, P. de Ruggiero, M. Migliaccio, S. Pierini, and G. Spezie, "X-band COSMO-SkyMed wind field retrieval, with application to coastal circulation modeling," *Ocean Sci.*, vol. 9, pp. 121–132, Feb. 2013.

[12] X. Li and S. Lehner, "Algorithm for sea surface wind retrieval from TerraSAR-X and TanDEM-X data[J]," *IEEE Trans. Geosci. Remote Sens.*, vol. 52, no. 5, pp. 2928–2939, May 2014.

[13] Y. Ren, X. Li, and G. Zhou, "Sea surface wind retrievals from SIR-C/X-SAR data: A revisit," *Remote Sens.*, vol. 7, no. 4, pp. 3548–3564, Mar. 2015.

[14] Y. Ren, M. He, and S. Lehner, "An algorithm for the retrieval of sea surface wind fields using X-band TerraSAR-X data," *Int. J. Remote Sens.*, vol. 33, no. 23, pp. 7301–7336, Dec. 2012.

[15] T. Shimada, H Kawamura, and M. Shimada, "An L-band geophysical model function for SAR wind retrieval using JERS-1 SAR," *IEEE Trans. Geosci. Remote Sens.*, vol. 41, no. 3, pp. 518–531, Mar. 2003.

[16] X. Zhou, J. Chong, X. Yang, W. Li, and X. Guo, "Ocean surface wind retrieval using SMAP L-band SAR," *IEEE J. Sel. Topics Appl. Earth Observ. Remote Sens.*, vol. 10, no. 1, pp. 65–74, Jan. 2017.

[17] D. R. Thompson, T. M. Elfouhaily, and B. Chapron, "Polarization ratio for microwave backscattering from the ocean surface at low to moderate incidence angles," in *Proc. IEEE Geosci. Remote Sens. Symp.*, 1998, pp. 1671–1673.

[18] Q. Xu, H. Lin, L. Jiang, X. Yin, Q. Zheng, and Y. Liu, "SAR measurement of ocean surface wind using a physics model," in *Proc. IEEE Geosci. Remote Sens. Symp.*, 2008, pp. 420–423.

[19] G. R. Valenzuela, "Depolarization of EM waves by slightly rough surfaces," *IEEE Trans. Antennas Propagat.*, vol. 15, no. 4, pp. 552–557, Jul. 1967.

[20] G. R. Valenzuela, "Scattering of electromagnetic waves from a tilted slightly rough surface," *Radio Sci.*, vol. 3, no. 11, pp. 1057–1066, 1968.

[21] G. R. Valenzuela, "Theories for the interaction of electromagnetic and oceanic waves—A review," *Bound. Layer Meteorol.*, vol. 13, no. 1–4, pp. 61–85, Jan. 1978.

[22] H. L. Chan and A. K. Fung, "A theory of sea scatter at large incident angles," *J. Geophys. Res.*, vol. 82, no. 24, pp. 3 439–3 444, Aug. 1977.

[23] A. K. Fung and K. K. Lee, "A semi-empirical sea-spectrum model for scattering coefficient estimation," *IEEE J. Ocean Eng.*, vol. 7, no. 4, pp. 166–176, Oct. 1982.

[24] W. J. Plant, "A two-scale model for short wind-generated waves and scatteometry," *J. Geophys. Res.*, vol. 91, no. C9, pp. 10 735–10 749, 1986.

[25] W. J. Plant, "A stochastic, multiscale model of microwave backscatter from the ocean," *J. Geophys. Res.*, vol. 107, no. C9, Sep. 2002, Art. no. 3120.

[26] M. A. Donelan and W. J. Pierson, "Radar scattering and equilibrium ranges in wind-generated waves with application to scatterometry," *J. Geophys. Res.*, vol. 92, no. c5, pp. 4 971–5 029, May 1987.

[27] P. A. Hwang, B. Zhang, J. V. Toporkov, and W. Perrie, "Comparison of composite Bragg theory and quad-polarization radar backscatter from RADARSAT-2: With applications to wave breaking and high wind retrieval," *J. Geophys. Res.*, vol. 115, Aug. 2010, Art. no. C08019, doi:10.1029/2009JC005995.

[28] X. Zhou, J. Chong, H. Bi, X. Yu, Y. Shi, and X. Ye, "Directional spreading function of the gravity-capillary wave spectrum derived from radar observations," *Remote Sens.*, vol. 9, Apr. 2019, Art. no. 361, doi: 10.3390/rs9040361.

[29] L. C. Morena, K. V. James, and J. Beck, "An Introduction to the RADARSAT-2 mission," *Can. J. Remote Sens.*, vol. 30, no. 3, pp. 221–234, 2004.

[30] T. Elfouhaily, B. Chapron, K. Katsaros, and D. Vandemark, "A unified directional spectrum for long and short wind-driven waves," *J. Geophys. Res.*, vol. 102, no. c7, pp. 15 781–15 794, Jul. 1997.

[31] T. Meissner and F. J. Wentz, "The complex dielectric constant of pure and sea water from microwave satellite observations," *IEEE Trans. Geosci. Remote Sens.*, vol. 42, no. 9, pp. 1836–1849, Sep. 2004.

[32] C. Cox and W. Munk, "Measurement of the roughness of the sea surface from photographs of the sun's glitter," *J. Opt. Soc. Amer.*, vol. 44, no. 11, pp. 838–850, Nov. 1954.

[33] B. R. Thomas, E. C. Kent, and V. R. Swail, "Methods to homogenize wind speeds from ships and buoys," *Int. J. Climatol.*, vol. 25, no. 7, pp. 979–995, Jun. 2005.

[34] X. Ye *et al.*, "Satellite SAR observation of the sea surface wind field caused by rain cells," *Acta Oceanol. Sin.*, vol. 35, no. 9, pp. 80–85, Sep. 2016.

[35] M. Lin, X. Ye, and X. Yuan, "The first quantitative joint observation of typhoon by Chinese GF-3 SAR and HY-2A microwave scatteromete," *Acta Oceanol. Sin.*, vol. 36, no. 11, pp. 1–3, Nov. 2017.

[36] X. Ye *et al.*, "A typhoon wind-field retrieval method for the dual-polarization SAR imagery," *IEEE Geosci. Remote Sens. Lett.*, vol. 16, no. 10, pp. 1511–1555, Oct. 2019.

[37] X. Liu, Q. Zheng, R. Liu, D. Wang, J. H. Duncan, and S.-J. Huang, "A study of radar backscattering from water surface in response to rainfall," *J. Geophys. Res.*, vol. 121, no. 3, pp. 1546–1562, Mar. 2016.

[38] X. Liu, Q. Zheng, R. Liu, M. A. Sletten, and J. H. Duncan, "A model of radar backscatter of rain-generated stalks on the ocean surface," *IEEE Trans. Geosci. Remote Sens.*, vol. 55, no. 2, pp. 767–776, Feb. 2017.

Xiaomin Ye received the B.S. degree in optical information science and technology from Nankai University, Tianjin, China, in 2006, the master's degree in physical oceanography from the First Institute of Oceanography, State Oceanic Administration, Qingdao, China, in 2009, and the Ph.D. degree in oceanic detection technology from the Ocean University of China, Qingdao, China, in 2017.

He is currently a Designer in charge of data processing for the Chinese HY-1C/D satellite with National Satellite Ocean Application Service, Beijing, China. His research interests include microwave scattering from the ocean surface and the application of ocean satellite data.

Mingsen Lin (Member, IEEE) received the B.S. degree in applied mechanics from National University of Defense Technology, Changsha, China, in 1984 and the Ph.D. degree in computational mathematics from the Computing Center, Chinese Academy of Sciences, Beijing, China, in 1992.

He was a Deputy Chief Designer of the ground application system for HY-1 and HY-2 satellites, where he organized the framework for the Chinese Ocean Satellite outline, and managed the construction of the ground application system for the Chinese Ocean Satellite with National Satellite Ocean Application Service, Beijing, China. He is one of the founders of satellite ocean remote sensing in China. He plays an important role in the development of Chinese ocean satellite and manned space flight. His research interests include ocean satellite data processing, remote sensing of the ocean, and their applications.

Qingtao Song received the B.S. degree in atmospheric sciences from Peking University, Beijing, China, in 1996 and the Ph.D. degree in oceanography from the University of Rhode Island, Kingston, RI, USA, in 2006.

He is currently a Research Scientist with the National Satellite Ocean Application Service, Beijing, China. His research interests include microwave scatterometry and radiometry and its applications in small-scale air–sea interactions.

Qimao Wang received the B.S. degree in oceanography from Ocean University of China, Qingdao, China, in 1985.

He is the Deputy Director of National Satellite Ocean Application Service, Beijing, China. He is currently a Research Scientist and plays important role in the operational application of ocean remote sensing in China. His research interests include the inversion of sea surface temperature and ocean applications with satellite data.